Exploring Hydrogen Hydrates at High-Pressure from Large Icy Moons to Ocean-Planets: New Phases and Elastic Properties at Ambient Temperature

L Andriambariarijaona, T Poręba, S Di Cataldo, R Gaal, U Ranieri, M Santoro, T Hansen, G Tobie, L E Bove

Exploring Hydrogen Hydrates at High-Pressure from Large Icy Moons to Ocean-Planets: New Phases and Elastic Properties at Ambient Temperature

L. Andriambariarijaona,[1,2] T. Poręba,[3] S. Di Cataldo,[1] R. Gaal,[3] U. Ranieri,[1,4] M. Santoro,[5,6] T. Hansen,[7] G. Tobie,[8] and L.E. Bove[1,2,3]

[1] *Dipartimento di Fisica, Sapienza Universitá di Roma, 4 Piazzale Aldo Moro, 00185 Roma, Italy*
[2] *Institut de Minéralogie, de Physique des Matériaux et de Cosmochimie (IMPMC), Sorbonne Université, CNRS UMR 7590, MNHN, 4, place Jussieu, Paris, France*
[3] *Laboratory of Quantum Magnetism, Institute of Physics, École Polytechnique Fédérale de Lausanne, CH-1015 Lausanne, Switzerland*
[4] *Centre for Science at Extreme Conditions and School of Physics and Astronomy, University of Edinburgh, EH9 3FD, Edinburgh, UK*
[5] *Consiglio Nazionale delle Ricerche, Istituto Nazionale di Ottica, CNR-INO, Via Nello Carrara 1, 50019 Sesto Fiorentino, Italy*
[6] *European Laboratory for Non Linear Spectroscopy, LENS, Via Nello Carrara 1, 50019 Sesto Fiorentino, Ita*
[7] *Institut Laue Langevin, Grenoble, France*
[8] *Univ Angers, Le Mans Université, CNRS, Laboratoire de Planétologie et Géosciences, UMR 6112, Nantes Université, 2 rue de la Houssinière, Nantes, 44322, France*

Hydrogen hydrates, formed from hydrogen and water under high-pressure and low-temperature conditions, present significant implications for both energy storage and planetary science. Hydrogen-filled ices are of particular interest in the context of icy celestial bodies, where extreme conditions favor their formation. This study investigates the complex phase diagram of hydrogen hydrate across a pressure range up to 70 GPa, utilizing angle-resolved neutron and X-ray diffraction techniques. We focus on the behavior of key phases: C_1, C_2, and C_3, highlighting the evolution of their crystallographic structures and elastic properties. Our findings reveal critical insights into phase transitions, structural deformations, and the stability of these hydrates, essential to quantify the role of hydrogen on the thermal state and chemical evolution of water-rich worlds of various sizes. The amount of hydrogen stored in the form of high-pressure hydrogen hydrate in their icy interior may condition their oceanic chemistry and their climate stability.

I. INTRODUCTION

Hydrogen and water, though poorly miscible under ambient conditions, form a variety of inclusion compounds at high pressures (HP) and low temperatures (LT). These hydrogen hydrates hold significant interest not only for their potential in large-scale energy storage—with theoretical hydrogen densities reaching up to 5 wt % at moderate pressures— [1] but also for their implications in planetary sciences in particular for large icy worlds in the outer solar system [.e.g. 2] and ocean planets around other stars [.e.g. 3]. These planetary bodies may contain a large fraction of water, potentially up to 50% of their total mass. They may also contain a significant fraction of hydrogen resulting from serpentinization and/or organic matter degradation [4–6]. The pressure at the base of their hydrosphere may range from 1-2 GPa for the large icy moons (Callisto, Titan, Ganymede) [2], to several tens of GPa for Earth-sized water-rich planets [7]. These implies that hydrogen released from the deep interior during planetary differentiation and subsequent evolution should be incorporated in the form of high-pressure hydrogen hydrate [8, 9]. It is therefore essential to probe the equation of state (EOS), stability, and elastic properties of hydrogen hydrates across a wide pressure range to evaluate their potential impact on the thermo-chemical evolution of these water-rich bodies. Hydrogen is a key proxy of hydrothermal activity and hence a potential driver for the emergence of life in icy worlds [4, 10]. Massive releases of hydrogen from planetary interiors can strongly impact the atmospheric greenhouse effect and extend the habitable zone far beyond the "classical" habitable zone, commonly defined for CO_2-dominated greenhouse atmosphere [11]. Above a critical threshold partly controlled by the amount of hydrogen in the atmosphere, runaway greenhouse may total change the thermal state of the planet, transitioning abruptly from one state dominated by liquid water and high-pressure ices at moderate temperatures to one dominated by hot supercritical water [12]. Recent observations by James Webb Spatial Telescopes provide the first observational constraints of "Hycean" worlds, consisting of a relatively thin H_2-dominated atmosphere overlying a liquid water ocean [e.g. 13, 14]. Thus, quantifying the amount of hydrogen that could be stored in the icy interiors and the rate at which it could be transported to the ocean and atmosphere is crucial to determine the thermal state and habitability of these water-rich worlds. A pre-requise to assess the role of hydrogen is a good knowledge of the stability and thermodynamics properties of hydrogen hydrate over a wide range of pressure.

The phase diagram of hydrogen hydrate is notably complex, consisting of multiple crystalline phases with varying molecular structures and stoichiometries (see

Figure 1). Above 0.1 GPa, H_2-H_2O system crystallizes into clathrate structure II (sII), characterized by a cubic unit cell ($Fd\bar{3}m$) that contains 16 small water cages and 8 large water cages encapsulating hydrogen molecules at variable amount (from 1 to 4 maximum occupancy) [15, 16]. As pressure increases to 0.5 GPa, the sII clathrate transitions into a high-pressure phase known as C_0 [17–20].

The C_0 phase is composed of interpenetrating spiral chains of hydrogen-bonded water molecules forming the proton disordered ice-XVII lattice [18, 19]. The hydrogen molecules sit in the crystal's spiral channels, aligned along the c-axis, and are orientationally disordered [18, 19]. This phase belongs to the space group $P3_221$, though it may transition to $P32$ depending on the hydrogen arrangement.

With further compression, structural transitions occur at 0.8 and 2.2 GPa, to the C_1 [20, 21] and C_2 phases, respectively. The C_1 phase adopts a rhombohedral lattice (space group $R\bar{3}$), with a water framework coinciding with ice-II and a 6:1 water-to-hydrogen ratio [22]. A proton-disordered variant of C_1, named C_1', was recently synthesized at 1.2 GPa and 298K (space group $R\bar{3}c$) [23].

In contrast, the C_2 phase, which is stable above 2.2 GPa, is characterized by two interpenetrating diamond lattices-one made of proton-disordered H_2O, the other of rotationally disordered hydrogen—resulting in a 1:1 ratio and crystallizing in the $Fd\bar{3}m$ space group. At pressures exceeding 30 GPa and ambient temperature, a notable splitting of diffraction lines indicates the emergence of a new tetragonal distortion of phase C_2, followed by another transition to a denser phase around 60 GPa[21, 24–27].

Recently, a transition from C_2 to an isostructural C_3 [28] phase, with a 2:1 hydrogen-to-water ratio, was reported to occur at about 40 GPa [9]. Unlike other phases, C_3 formation requires thermal activation to overcome kinetic barriers [9]. This phase has been observed to persist up to at least 90 GPa.

In this study, we explore the phase diagram of hydrogen hydrate in the 1 to 50 GPa range using angle-resolved neutron and X-ray diffraction techniques. In particular, we focused on the behaviour under pressure of phases C_1, C_2 and C_3, whose crystallographic structures are shown in Figure 1. This enabled us to determine their elastic properties, re-evaluate their phase boundaries, and gain insights into pressure-induced structural deformations.

II. EXPERIMENTAL DETAILS

A. Sample preparation

All hydrogen hydrate (H_2-H_2O, H_2-D_2O or D_2-D_2O) samples of this study were initially prepared following the same procedure in the form of clathrate sII. Preparations were performed at the Helmholtz-Centre Berlin (Germany) by exposing ice spherical crystallites at 244 K to H_2 or D_2 gas at 0.28 GPa for typically 20–30 min. Ice spheres with typical diameter of several 10μm were formed by spraying D_2O water directly into liquid N_2. To limit contamination with H_2O frost, the spraying was performed in a sealed glovebox under an inert N_2 atmosphere.

B. Neutron diffraction experiments

Neutron diffraction is likely the most effective technique for studying the structure of hydrogen-containing crystals. However, in practice, deuterated analogues are typically used to minimize the significant incoherent scattering of hydrogen, which gives rise to significant background noise in the diffraction pattern. The deuterated sII sample of about 30 mm^3 was loaded cryogenically (80 K) into a toroidal TiZr gasket along with a Pb chip (pressure marker) inside the locking clamp device of the Paris-Edinburgh press. Subsequently, the clamp was tightened to exert pressure on the sample and then transferred into the press [29]. The press was cooled by two-stage closed-cycle refrigerator in an "orange" cryostat. The neutron diffraction data was collected at the

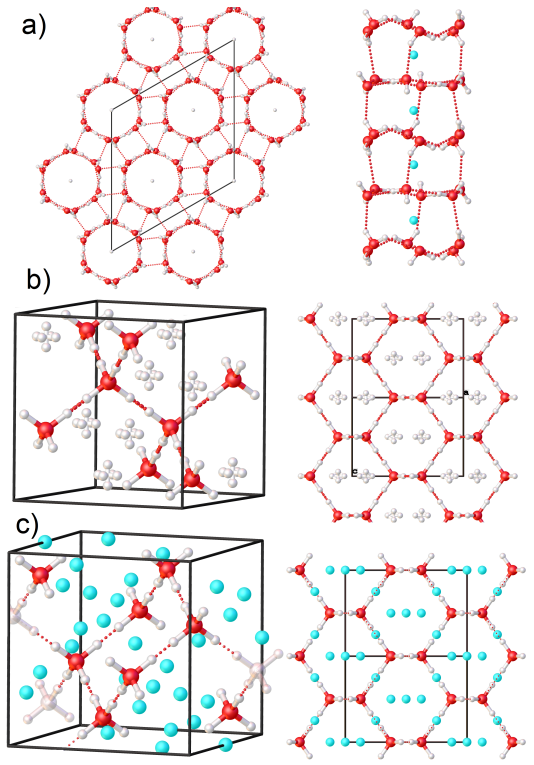

Figure 1. Crystal structures of hydrogen hydrates. a) (left) C_1 structure viewed along [001] and (right) hydrogen-bonded water channels . (b-c) Unit-cell packing in C_2 and C_3, with the respective views along the [110] on the hydrogen-filled hexagonal channels (right). Note that hydrogen molecules in C_1 and C_3 are orientationally-disordered (cyan spheres)

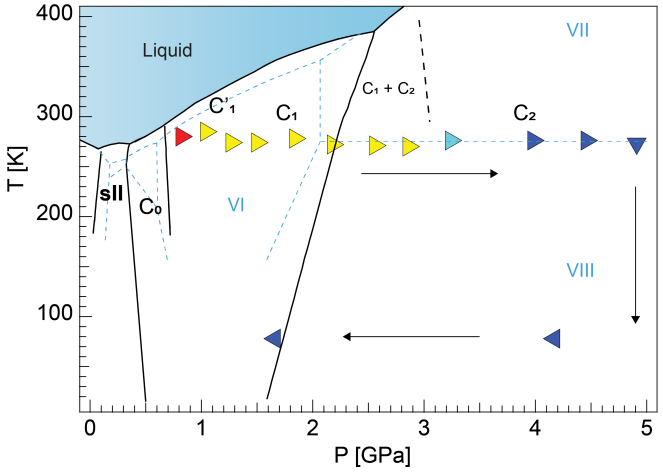

Figure 2. Phase diagram of H_2-H_2O superimposed on those of pure H_2O for P < 5GPa. Black solid lines are the H_2-H_2O phase equilibrium lines proposed in Ref [31, 32], while blue dashed lines correspond to phase transitions in H_2O [33]. The dashed black line indicates a region of C_1 + C_2 coexistence observed by Ref [31]. The triangles show the experimental P-T points taken during neutron diffraction in this study. The colours represent the phases observed: red for SII, yellow for C_1, light blue for C_1 + C_2 coexistence, and dark blue for C_2.

high-intensity diffractometer D20 at the Institut Laue-Langevin (Grenoble, France), using a wavelength of 1.54 Å. The thermodynamic points shown in Figure 2.[30] have been explored.

C. Synchrotron X-ray diffraction experiments

For the X-ray diffraction (XRD) experiments, we used diamond anvil cells (DAC) equipped with diamond anvils of 250/300 μm culet diameters and 200 μm thick Re foils as gaskets. Gaskets were pre-indented and drilled with a hole of 90 μm radius to serve as a sample chamber. The H_2-H_2O samples were prepared and cryoloaded in the DAC with the same methods as described in Refs [9, 34]. A small amount of sample was placed into the gasket hole of the DAC partially immersed in a liquid nitrogen bath. The DAC was then rapidly closed and a sufficient load was applied at about 78 K to ensure that the sample is sealed at pressures above 0.3 GPa before warming up to 300 K. Angular dispersive X-ray diffraction experiments were conducted at the PSICHE beamline of the SOLEIL synchrotron facility (Paris, France) and at the ID27 beamline at the European Synchrotron Radiation Facility (ESRF) in Grenoble, France. The X-ray wavelength was 0.3738 Å (33 keV) for both PSICHE and ID27. The beam spot size was 10 × 10 μm^2 at PSICHE and 0.3 × 0.25 μm^2 at ID27, respectively. Diffraction images were recorded using flat-panel detectors: a Dectris Pilatus 2M CdTe at PSICHE and an EIGER2X CdTe 9M at ID27. The detector distance, tilt, and the position of the X-ray beam were calibrated with a CeO_2 standard.

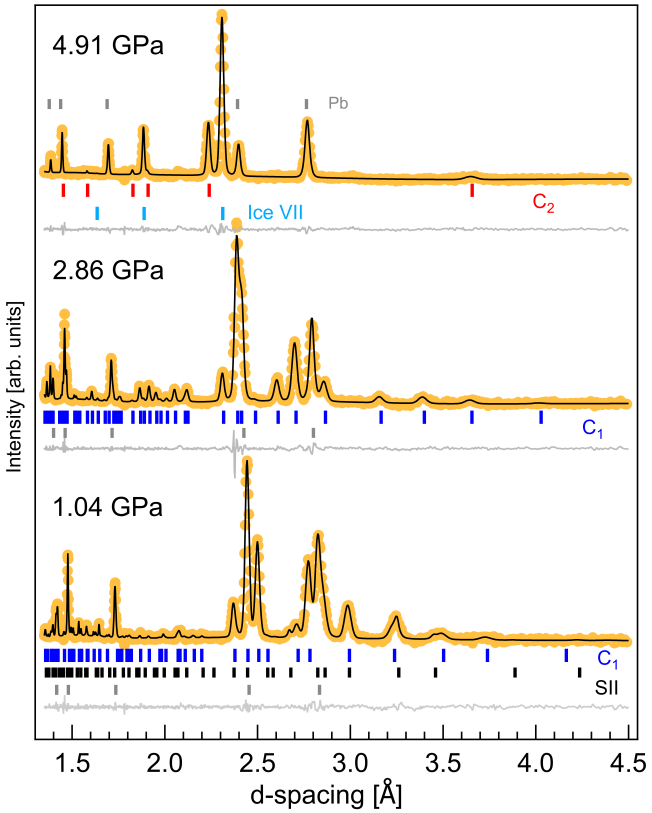

Figure 3. Representative neutron powder diffraction patterns (λ = 1.54 Åupon compression between 1.04 and 4.91 GPa .The observed data are shown as dots and the calculated profile as a solid line. The tick marks denote the calculated positions of the diffraction peaks for SII (black),C_1 (blue), C_2 (red), ice VII (cyan) and lead (grey).

X-ray image integration was performed using the DIOPTAS [35], while Le Bail refinements of the diffraction patterns were carried out with the FULLPROF [36]. Pressure during the XRD measurements was determined using the equation of state for gold, as outlined in Ref.[37].

III. RESULTS AND DISCUSSION

IV. EOS OF C1

Figure 3 shows a selection of the neutron diffraction patterns collected during compression at about 295 K. At 1.04 GPa, diffractogram shows the coexistence of SII and C_1 phases. Lack of C_0 phase is in accordance to volumetric studies [20], which determined the C_0-C_1 phase transition pressure at 0.86 GPa at 291 K. The presence of SII can be explained by a kinetically-hindered transition from SII to C_1, and fast compression directly into the region where C_0 is already destabilized (P > 0.8 GPa) [20]. By gradually increasing the pressure, the SII phase disappears at 1.27 GPa, and only C_1 phase persists up to 2.86 GPa. When the pressure is increased to 3.24

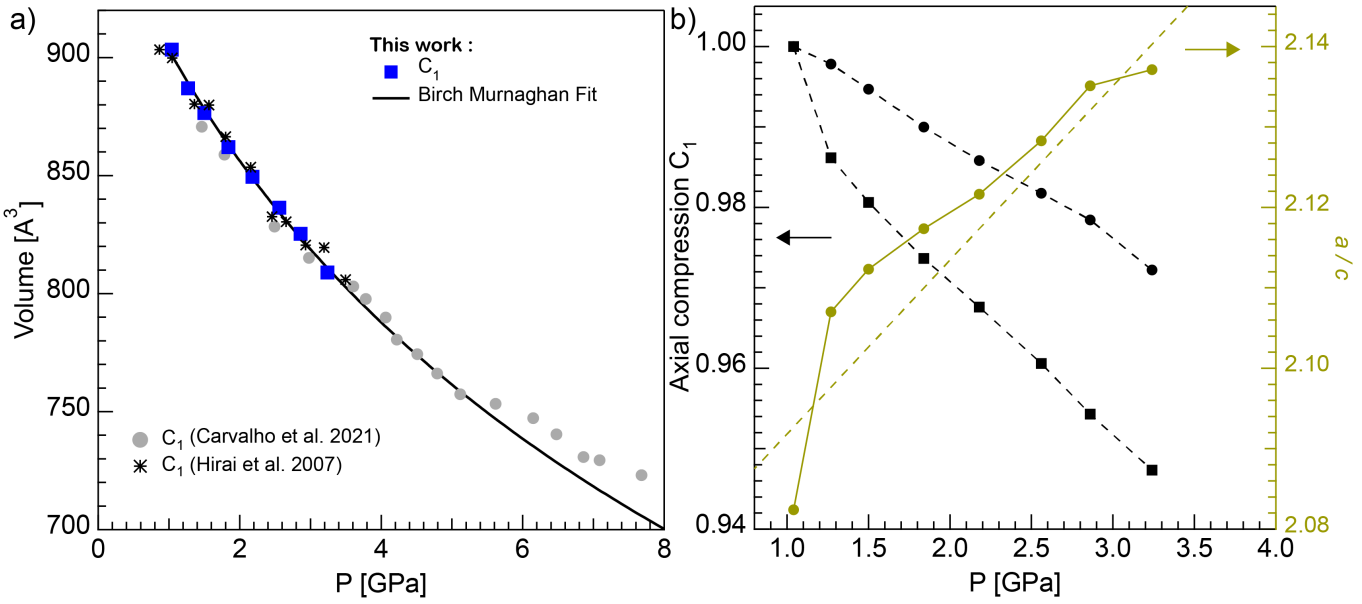

Figure 4. a) Pressure dependence of the unit cell volume of C_1. The symbols represent experimental volumes: solid squares correspond to data from this study, while circles and stars denote data from Refs.[38, 39] (in Ref [39] the data were collected at 200 K, with metastable C_1 preserved at higher pressures). The solid curve is a fit to our data using the second-order Birch-Murnaghan equation of state. b) (left axis) Evolution of the normalized lattice parameters of the C_1 unit cell with pressure. The circle and square symbols indicate the behavior of the a and c axes, respectively. Dashed lines are added as visual guides. (right axis) The green circles represent the pressure dependence of the a/c ratio in the C_1 phase, with the green dashed line showing a linear extrapolation of the a/c ratio in pure ice II. The equation for the extrapolation is: 0.216xP + 2.07, based on data plotted from Fortes *et al.* [40].

GPa, we observe a transition from phase C_1 to phase C_2, whereas the two phases coexist at this pressure. Further compression to 3.98 GPa results into the complete transformation of C_1 into C_2. The presence of ice VII on the diffractogram is explained by the change in stoichiometry between phase C_1 (6:1) and phase C_2 (1:1). This change implies an excess of water that cannot be incorporated into C_2 structure. This excess water reorganizes into ice VII, the stable phase at these conditions. Further compression to 4.94 GPa, the maximum pressure reached during this neutron experiment, C_2 is the only stable phase observed.

The measured unit cell volume of C_1 derived from Rietveld refinements is represented in Figure 4a as function of pressure, and compared to the one derived from x-ray powder data collected in a DAC between 0.8 and 3.5 GPa at 300 K by Hirai and co-workers [38], and the one recently derived from neutron powder diffraction data between 1.1 and 7.8 GPa at 200 K by Carvalho *et al.* [39]. In this last experiment the C_1 phase cohexisted from 3 GPa up to 7.8 GPa with the C_2 phase without never achieving a complete transition, likely due to the low temperature, while at room temperature coexistence is observed in a narrower pressure range between 3.2 GPa and 3.5 GPa [38]. The low-temperature effect on the stability of C_1 phase can be linked to the hydrogen immobility due to solidification above 3 GPa at 200 K [41]. In the overlap region the three sets of data (Figure 4) are in a very good agreement. Notably, the minimal impact of cooling from 300 to 200 K on the material's contraction stands out. Our P-V data fitted with a third-order Birch-Murnaghan (BM3) equation of state, yields a zero-pressure unit-cell volume,V_0 = 960.44 (11) Å^3 , a zero-pressure isothermal bulk modulus, B_0= 14.52 (4) GPa, and a first pressure derivative of the bulk modulus, B' = 3.3 (2). However, the relatively narrow pressure range over which the measurements were carried out gives unconstrained values for the three parameters, which are highly correlated. Setting the parameter B' to 4, as suggested by previous studies [38, 39] gives a V_0 = 962 (4) Å^3 and B_0= 13.6 (5) GPa. The bulk modulus of hydrogen-filled ice C_1 is slightly higher than that reported for ice II [40] (B_0=12.13 (7)), a phase that shares the same water sublattice as C_1. Therefore, in the C_1 structure, the presence of hydrogen slightly strengthens the structure due to steric repulsion between the host and guest molecules. The extrapolation of the V(P) curve at high pressure shows a good agreement with the data from reference [39] up to 5 GPa; above this value, a progressive deviation is observed. This suggests that low temperatures allow the C_1 structure to be preserved in the pristine state up to at least 5 GPa. The departure from the extrapoleted EoS values for pressures above 5 GPa is likely related to lowering precision of the determination of the lattice metrics both due the overlap between the Bragg reflections from C_1 and C_2 coupled with increasing peak

width, and because of diminishing signal from C_1 as it is being consumed to form C_2 upon compression.

Unit cell parameters determined at each pressure are plotted in Figure 4. The compression of the structure is strongly anisotropic, achieved through the drastic shortening of the c axis (22(1) TPa^{-1}) relative to the a axis (12.4(3) TPa^{-1}). Such anisotropy of the linear compressibility was also observed in ice II (29.8(3) and 20.0(4) TPa^{-1}) at 225 K and attributed to the columnar structure of ice II (see Figure 4b), where the strongly hydrogen-bonded water hexamers lie in (001) [40]. They are, in turn, stacked in the perpendicular direction, along the crystallographic c axis. In C_1 structure stacking is stabilized by weaker hydrogen bonds between hexamers, with less favourable geometry, than in ice II. Additionally, the higher compressibility along [001] can be ascribed to the geometrical flexibility of the puckered water hexamers, which can assume planar geometry upon compression, at the expense of volume reduction. Higher anisotropy of the smaller linear compressibilities in C_1 with respect to ice II is a direct consequence of water channel filling. Hydrogen molecules in C_1 form short repulsive intermolecular contacts to the neighbouring water molecules , which limits the structure compression in the crystallographic a direction (in-plane directions), permitting higher hydrogen mobility along the channel (crystallographic c direction). Center of mass of the disordered hydrogen-molecules (Figure 2) form shorter Van der Waals contacts to the channel walls (2.74(1)Å at 1.4 GPa) than between each other (3.01(1)Å at 1.4 GPa), close to their sum of Van der Waals radii of 2.72 and 2.40Å, respectively [42]. In fact, molecular dynamics simulations and Raman spectroscopy confirm that hydrogen molecules in C_1 lie in the center of the hexagonal cavity and are likely orientationally disordered. [31, 43].

V. EOS OF C2

X-ray diffraction powder measurements in diamond anvil cell (DAC) have been employed to determine the molecular volume of H_2 –H_2O hydrates above 5 GPa and up to 50 GPa. Representative diffraction patterns at 5, 26.6, 38.1, and 46.3 GPa are shown in Figure 5a. For pressures below 30 GPa (P < 30 GPa), all diffraction lines are well indexed with the C_2 cubic structure plus ice VII structure which formed during C_1 to C_2 transition due to the relevant change in stoechiometry of the hydrate (1:6 H_2 to H_2O ratio in C_1; 1:1 in C_2). Conversely, above 30 GPa we observe systematic deviations in the positions and profiles of peaks when adjusting XRD diagrams to a cubic model. This divergence is primarily evidenced by the Bragg features at approximately 11° and 13.5°, where a split is observed for the (2 2 0) and the (3 1 1) reflections, which is not accounted for by the cubic C_2 model ($Fd\bar{3}m$) (see Figure 5b). This splitting persists up to the maximum pressure reached in this experiment.

A similar splitting was observed also in previous studies [9], and we can safely exclude it is due to deviatoric stress in the sample chamber or to pressure gradient as in such a case it would also affect ice VII reflections [21, 26]. To obtain more information on the nature of this transition, we relied on theoretical predictions from first-principles molecular dynamic simulations. Theoretical calculations predict that, in this range of pressures, the cubic structure is no longer stable and it will transform into the one of the three energetically favourable orthorhombic structures: $P4_12_12$, $I4_1/amd$ and $Pna2_1$ [9, 25, 28]. It should be noted that these structures have very similar enthalpy and differ only in minor orientation differences between the water frame and the guest hydrogen molecules. We refined the experimental diffractograms accordingly (see Figure 5b) and a good agreement was observed for all three structures, which yield to similar lattice parameters (see table), with a significantly higher agreement factor for $I4_1/amd$ compared to $P4_12_12$ and $Pna2_1$, despite its higher symmetry. Indeed, the $P4_12_12$ and $Pna2_1$ models predict additional symmetry-unrelated peaks that are not observed experimentally (see Figure 5c). These peaks may have very low intensities due to minor structural distortions, placing their signals at the noise level. Therefore, drawing definitive conclusions based solely on this observation is challenging. However, since the transition stems from a distortion of the cubic lattice, the resulting tetragonal structure should exhibit relatively high symmetry, corresponding to $I4_1/amd$. Among the three proposed space groups, only $I4_1/amd$ is a maximal subgroup of $Fd\bar{3}m$, suggesting a non-displacive phase change mechanism, as indicated by the continuous compression trend, as observed in this study. The $I4_1/amd$ space group is here chosen as the appropriate subgroup for the distorted C_2 phase, in the following named C_2'. The XRD patterns were further analyzed using this space group.

The variation in lattice parameters values of the C_2 and C_2' structures as a function of pressure is presented in Figure 5c together with the predictions of [9] using the $Pna2_1$ model structure and simulated $I4_1/amd$. The unit-cell axis ratio changes with increasing pressure, with the c-axis being less compressible than the a-axis. This can be explained looking at the orientational order of hydrogen molecules within the structures [9]. Initially, H_2 molecules are randomly oriented, and the compression is isotropic, according to the crystal symmetry. When the pressure aproaches 30 GPa, orientational ordering of H_2 molecules and alignment along the c-axis can be observed, making compression in this direction harder [9]. The pressure at which we observe the tetragonal distortion nicely corresponds to the pressure where previous theoretical calculations indicated H_2 molecules alignment [9, 25].

Figure 8 shows the measured unit cell volume of the C_2 and C_2' as a function of pressure in the range 4 to 47 GPa obtained from both our neutron and X-ray diffraction experiments, compared to previous literature data [9, 24, 26, 38]. The measured unit cell volume con-

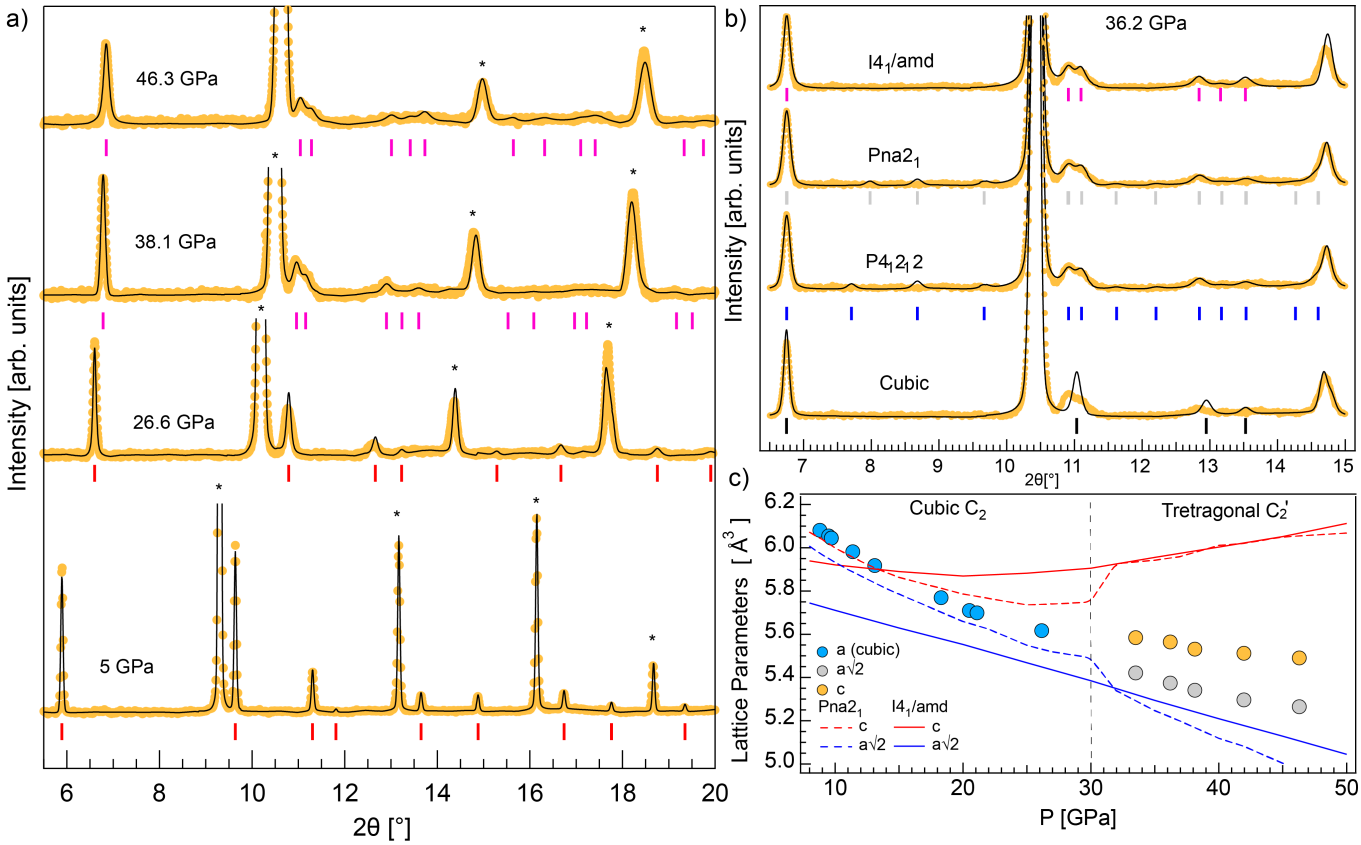

Figure 5. a) Representative X-ray diffraction patterns of C_2 measured during compression. The ticks correspond to Bragg reflections: (red) for the cubic $Fd\bar{3}m$ structure and (magenta) for the $I4_1/amd$ structure. For clarity, the ice VII peaks are marked with a star, and the most intense reflection (110) is not fully displayed. b) Comparison of the LeBail fitting performed on the experimental data at 36.2 GPa, when splitting is observed. From bottom to top, the diffractogram was fitted with the cubic structure ($Fd\bar{3}m$), as well as with the structures predicted by calculations: $P4_12_12$, $Pna2_1$, and $I4_1/amd$. c) Variation of lattice parameters as a function of pressure at 300 K, compared with the results of calculations performed in Ref.[9] on the $Pna2_1$ (dashed line) and $I4_1/amd$ (solid line). The circles represent the experimental lattice parameters. In the tetragonal phase, a is multiplied by $\sqrt{2}$. The dotted lines represent the parameters according to the simulation. The shaded area corresponds to the regions where the H_2 molecules align and order along the c-axis.

tinuously decreases with pressure up to 30 GPa, above which a change in the slope is observed. As can be observed our data agree with those reported by Hirai *et al.*

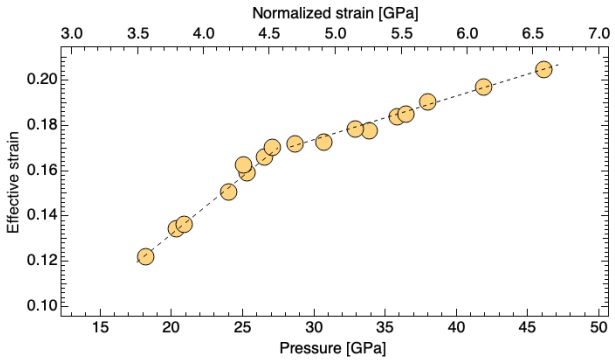

Figure 6. Normalized stress-strain plot for C_2 in the region of onset of the tetragonal distortion.

and Ranieri *et al.*, while, the ones reported by Machida *et al.* are systematically larger for pressures above 20 GPa. The origin of this difference could reside in a different filling ratio of the starting hydrate material or in a more anisotropic compression, due to the lack of pressure transmitting medium, which might delay the transition to the C_2' phase. Our data can be fitted below 30 GPa using a (BM3) equation of state, which yields to a V_0 of 325.43 (9) Å^3, B_0 of 10.10 (2) GPa, and B_0' of 4.53 (1). The bulk modulus we obtained is significantly lower than the values reported by Vos *et al.* (V_0 = 304 Å^3, B_0=15.6 GPa, and B_0'=4.3) [21]. This can be due to the fact that Vos *et al.* fitted the full range of their P-V x-diffraction data up to about 50 GPa, thus including the pressure regime where we observe deviation from the cubic structure. For comparison, the parameters for ice VII derived by neutron diffraction in the 1 to 14 GPa range are: V_0 = 42.25 Å^3, B_0=13.8 GPa, and B_0'=5.9 [44]. Therefore, the bulk modulus of C_2 is lower than that of ice VII, in-

dicating that hydrogen hydrate is more compressible and less resistant to pressure than the homologous pure ice phases, likely due to the fact that one of the two sublattices is made by non-bonded hydrogen molecules.

To fit the data > 30 GPa, we used a modified BM by using P_R and V_R as the starting point, instead of (P_0 and V_0).

$$P(V) = P_r + \frac{3B_r}{2}\left[\left(\frac{V_r}{V}\right)^{7/3} - \left(\frac{V_r}{V}\right)^{5/3}\right]\left\{1 + \frac{3}{4}(B'_r - 4)\left[\left(\frac{V_r}{V}\right)^{2/3} - 1\right]\right\}$$

where P and V are the pressure and volume of the reference point and are set at 30 GPa and 170.5 Å^3 respectively. This approach gives a finite-pressure isothermal bulk modulus derivative B'_r of 4.2 (2) and a finite-pressure isothermal bulk modulus B_r of 185.66 (10) GPa. For comparison, the Bulk modulus of ice VII at 30 GPa is estimated to be around 150 GPa, using literature values ranging from 124 to 177 GPa [45–47]. However, these values are still lower than those observed for the C_2' phase, indicating that the C_2' phase is stiffer. This increased stiffness could be attributed to a specific molecular reorganization, leading to a more compact structure that is more resistant to compression. Additionally, the diffraction data for C_2' was fitted using 2nd order modified BM EOS model. For the phase appearing at high pressure, in order to estimate B_0 and B'_0, we replaced the classical F-f model with a corresponding linearized G-g strain-stress model, with an arbitrary value of V_0 [48] The ambient-pressure properties were then determined at $g = g_0$ using G-g relationships (see Figure 6). The stress-strain relation shows a nonlinearity around 29 GPa, confirming a formation of a solid with different elastic properties. Fitted EOS parameters for this high-pressure phase (C_2') results in B_0 = 80(1) GPa, B'_0= 4 and V_0=216.2(6).

VI. EOS OF C3

The H_2-H_2O sample was compressed to 40 GPa, a pressure at which the sample was moderately laser-heated (below 1200 K) using a CO_2 laser with 10.6 μm wavelength, following a similar methodology to Ranieri et al. [9]

The C_3 phase formed near the laser-heated spot, coexisting with a mixture of Ice VII and the C_2 phase (see Figure 7a). Both C_2 and C_3 phases share the same cubic space group $Fd\bar{3}m$, with the oxygen atoms located at 8*a* and the H_2 molecules located at 8*b* Wyckoff position for C_2 and 16*d* for C_3. Despite being described by the same space group, C_2 and C_3 are easily distinguishable due to their differing volumes. This difference is evident in the X-ray diffraction patterns obtained after laser heating (see Figure 7b)), taken at the intersection of the two phases where the lattice parameter a is 5.7863 Å is for C_3 compared to 5.35064 Å for C_2, a 21% volume difference. This considerable expansion is attributed to the substantial incorporation of H_2 molecules, which doubles in the C_3 phase compared to the C_2 phase.

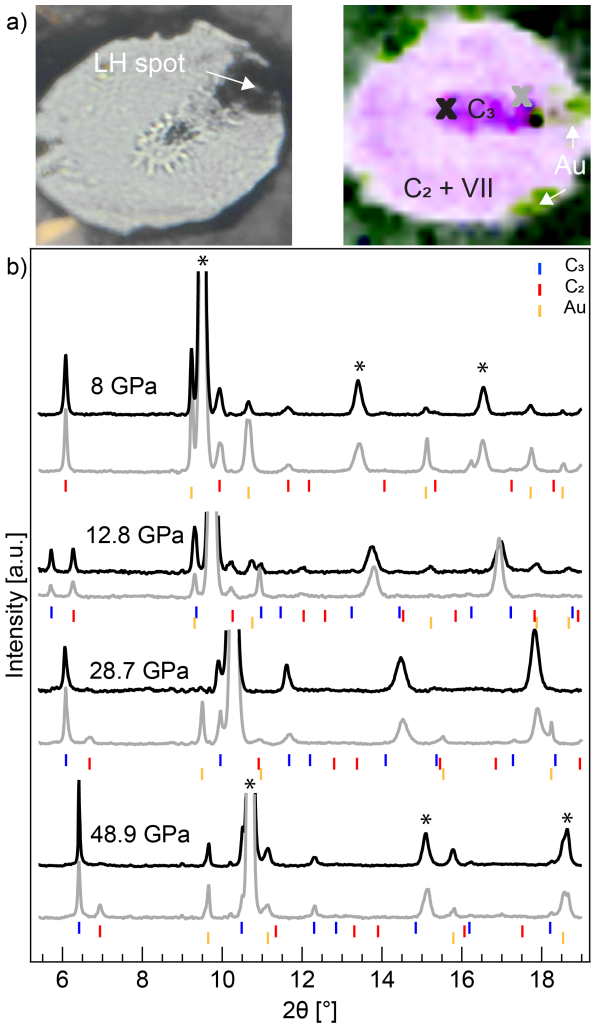

Figure 7. a) Photograph and X-ray mapping of the sample after laser heating, showing the formation of C_3 phase at the center, near to the heated spot. b) Representative X-ray diffraction patterns of the sample measured upon decompression after laser heating. The black and grey patterns correspond to the regions marked with crosses in Figure (a). The black patterns represents a region with a predominance of the C_3 phase, while the grey curve shows a zone where C_3 and C_2 coexist. The ticks correspond to the Bragg reflections of C_2, C_3 and gold (Au) structure. The ice VII peaks are indicated by a star. For clarity, only the diffraction patterns at 48.9 GPa and 8 GPa are annotated. In addition, the (110) reflections of ice VII is not plotted entirely.

The C_3 phase was here characterized by powder X-ray diffraction during the decompression of the laser-heated sample. As seen in Figure 7b, the diffraction lines of the C_3 solid were observed to shift continuously with pressure down to 12.8 GPa, suggesting the lack of a structural phase transition. At that pressure, however, there is a gradual drop in the intensity of the C_3 (110) diffraction line in favour of the (110) reflection of C_2. Below that pressure, at 8 GPa, the diffraction lines of C_3 are no longer detectable and only C_2 phase is visible in the

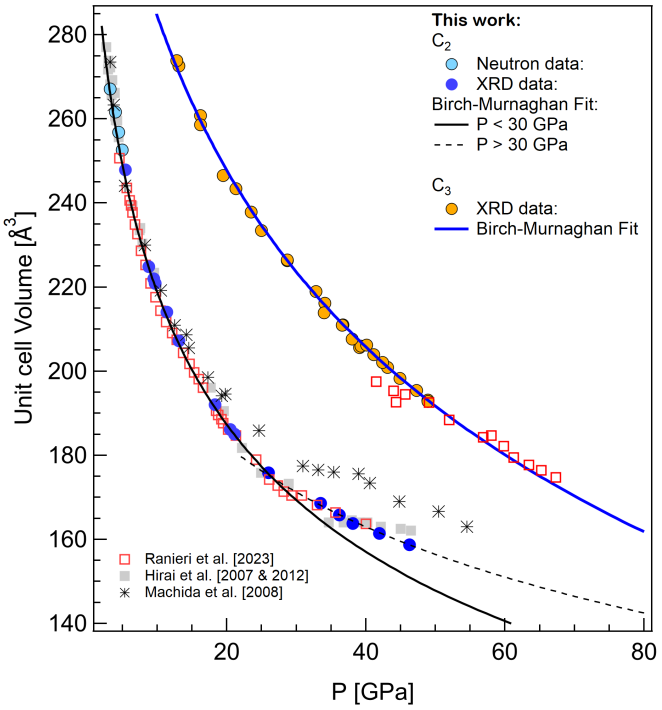

Figure 8. Pressure dependence of unit cell volume of C_2 and C_3. The black solid line is the Birch-Murnaghan fit to the data up to 30 GPa for C_2 and the blue line for C_3. Published x-ray data are for C_2 and C_3 are shown for comparison [24, 26, 38].

sample. This indicates the continuous decomposition of C_3 into C_2 and H_2. This also suggests that C_3 does not have a sufficiently high activation barrier to permit recovery in a metastable state below 10 GPa at ambient temperature.

The obtained volume-pressure data of C_3 from 48.9 GPa down to its decomposition pressure, can be found in Figure 8 where we include, for comparison the x-ray powder diffraction data by Ranieri *et al.* [9]. These data were obtained by a similar laser heating synthesis at 40 GPa, followed by compression from 40 to 80 GPa. The data fitted using a third-order Birch-Murnaghan equation of state provides values of V_0 = 372.11 (10) Å^3, B_0 = 23.72 (3) GPa, and B_0' = 3.6 (1)

In the overlap region, the Ranieri *et al.* data are slightly lower, presumably due to hydrogen mobility in the just-laser-heated samples, but at higher pressure, there is an excellent agreement with the exatrapolation of our determined equation of state.

VII. DISCUSSION AND CONCLUSIONS

The EOS data presented herein spans pressures from 1 GPa to 50 GPa, covering the range of pressures expected in hydrogen-rich and water-rich planetary environments, ranging from large icy moons of Jupiter and Saturn to sub-Neptune ocean-planets. Determining under which conditions hydrogen hydrates form and transforms to different phases is essential to assess the hydrogen inventory of these bodies and its possible impact on their thermal state and habitability. For large icy moons, like Ganymede, Callisto and Titan, their hydrospheres are expected to be divided in three main layers: an outer layer composed mostly of Ice Ih, a liquid water layer, containing unconstrained fractions of dissolved salts, organics and volatile compounds, and a thick high-pressure mantle, composed primarily of ice V and ice VI [2, 50]. The C_1 phase studied here is expected to be stable throughout the high-pressure ice mantle separating the ocean from the rocky core, and may transform into the C_0 phase in the uppermost part of the high-pressure ice mantle. Depending on the total fraction of hydrogen, the presence of C_1 phase and its phase transition to C_0 may affect the thermo-mechanical properties of this icy mantle and then dynamics of this layer. Future modeling works are needed to investigate their potential role.

At present, no water ice is expected at pressure than 2 GPa in these large icy moons [e.g. 2], therefore, no C_2 phase may exist in this moon. However, just after accretion, their inner core may have consisted of a undifferentiated rock-ice mixture [51–53] at pressure up to 5 GPa. In such conditions, any present hydrogen will be trapped in the form of C_2, and will progressively transform into C_1 as the interior differentiation progressively leads to a segregation of ice phases and rock minerals, corresponding to a upward migration of low density water-rich phases (including notably hydrogen hydrate) and downward migration of rock minerals. As the inner core progressively warms up from an initial temperature of 100-150K to the melting point of ice (300K-500K depending on pressure and composition) on a timescale of about 0.5-1 Gyrs, large quantities of hydrogen may be produced by aqueous alteration even at subsolidus tem-

Table I. All of the (EOS) parameters for the different phases of hydrogen hydrates (C_1, C_2 and C_3), determined in the present study and in the literature, include the volumes at zero pressure (V_0), the bulk moduli (B_0) and pressure derivative (B_0'). These values are compared with those found for pure water ice I_h, II and VII.

Phase	B_0 (GPa)	B_0'	V_0 (Å^3)	Ref.
C_1	13.60(5)	4.0(f)	962(4)	this study
	16.30(6)	4.0(f)	939(4)	(Carvalho *et al.*)[39]
C_2	10.10(2)	4.5(1)	325.43(9)	this study P< 32 GPa
	15.60(2)	4.3(6)	304	(Vos *et al.*)[21]
	15.70(10)	4.8(3)	304	(Hirai *et al.*)[26]
C_3	23.72(3)	3.6(1)	372.11(10)	this study
ice I_h	9.06(2)	4.0(f)	130.0(1)	(Gagnon *et al.*)[49]
ice II	12.79(8)	4.0(f)	306.9(2)	(Fortes *et al.*)[40]
ice VII	13.80(2)	5.9(1)	42.25(f)	(Klotz *et al.*)[44]

(f) Fixed value.

perature due to the likely presence of ammonia [54]. The C_2 phase and its transition to C_1 is therefore essential to understand the fate of hydrogen during the differentiation processes. Future experimental investigations and differientiation models are required to further determine the stability of these phases and the efficiency of hydrogen transport upward during the interior differentiation.

The physical properties of the C_1 phase, particularly its bulk modulus and compressibility, are key to understanding the convective dynamics within the interiors of icy moons. Our data show that hydrogen-filled ice, such as C_1, is slightly more resistant to compression than ice II. This suggests that hydrogen's presence strengthens the structure through steric repulsion between the host and guest molecules. Extrapolations of the volume-pressure relationship agree well with previous data up to 5 GPa but deviate at higher pressures, highlighting the likely non pristine nature of the metastably preserved C_1 phase. This increased stiffness at high pressures underscores the importance of C_1 in shaping the convective and tectonic processes within planetary interiors.

For the C_2 phase, our data show a distinct change in compressibility at 30 GPa where a transition to a denser, stiffer phase (C_2') occurs. The diffraction data show a gradual departure of the a/c ratio from unit and indicate C_2' as a different tetragonal phase. The bulk modulus of C_2 is lower than that of ice VII, indicating that this phase is more compressible, likely due to the presence of one single sublattices of hydrogen bonded water molecules. If we compare the bulk modulus to its pure ice counterparts, i.e. ice Ic, actually once again the hydrogen filled phase is stiffer. At pressures beyond 30 GPa, we observed a significant increase in stiffness in the C_2' phase, which may be due to the hydrogen nematic alignment along the c axis. This transition is critical for understanding how planetary interiors, particularly in larger icy bodies, respond to extreme pressures.

The C_3 phase, which forms only at high temperature and high pressure conditions, provides further insight into the behavior of hydrogen hydrates at extreme pressures. Our data show that this phase can be preserved during decompression down to 13 GPa, which remarkably expands the pressure range over which it is stable. The elastic properties of C_3 are particularly relevant for the study of ice giants like Uranus and Neptune, where pressures deep in the interiors likely exceed the threshold for C_3 formation. A direct comparison with the C_2 structure, which share the same water frame, indicates that the insertion of hydrogen molecules, at the expenses of lattice expansion, results in a markedly stiffer structure. The bulk modulus and compressibility of C_3 provide valuable data for understanding hydrogen sequestration in deep ice layers, a process that may significantly affect the internal structure and thermal evolution of these massive planets.

The detailed elastic property measurements and EOS data we obtained are essential for interpreting seismic and gravitational data, which are key to inferring planetary internal structures. The propagation of seismic waves and the variations in a planet's gravitational field are directly influenced by the material properties of hydrogen hydrates, making this study highly relevant for improving models of planetary composition and dynamics. By providing a better understanding of how hydrogen hydrates behave under extreme pressures, our findings contribute to refining planetary models and offer new insights into the evolution of hydrogen-rich planets and moons.

[1] P. Di Profio, S. Arca, F. Rossi, M. Filipponi, Comparison of hydrogen hydrates with existing hydrogen storage technologies: Energetic and economic evaluations, International Journal of Hydrogen Energy 34 (22) (2009) 9173–9180. doi:https://doi.org/10.1016/j.ijhydene.2009.09.056.
URL https://www.sciencedirect.com/science/article/pii/S0360319909014967

[2] B. Journaux, K. Kalousová, C. Sotin, G. Tobie, S. Vance, J. Saur, O. Bollengier, L. Noack, T. Rückriemen-Bez, T. Van Hoolst, et al., Large ocean worlds with high-pressure ices, Space Science Reviews 216 (2020) 1–36.

[3] A. Léger, F. Selsis, C. Sotin, T. Guillot, D. Despois, D. Mawet, M. Ollivier, A. Labèque, C. Valette, F. Brachet, et al., A new family of planets?"ocean-planets", Icarus 169 (2) (2004) 499–504.

[4] S. Vance, J. Harnmeijer, J. Kimura, H. Hussmann, B. DeMartin, J. M. Brown, Hydrothermal systems in small ocean planets, Astrobiology 7 (6) (2007) 987–1005.

[5] T. M. McCollom, F. Klein, M. Ramba, Hydrogen generation from serpentinization of iron-rich olivine on mars, icy moons, and other planetary bodies, Icarus 372 (2022) 114754.

[6] K. E. Miller, C. R. Glein, J. H. Waite, Contributions from accreted organics to titan's atmosphere: new insights from cometary and chondritic data, The Astrophysical Journal 871 (1) (2019) 59.

[7] L. Noack, I. Snellen, H. Rauer, Water in extrasolar planets and implications for habitability, Space Science Reviews 212 (2017) 877–898.

[8] H. Hirai, H. Kadobayashi, Significance of the high-pressure properties and structural evolution of gas hydrates for inferring the interior of icy bodies, Progress in Earth and Planetary Science 10 (1) (2023) 3. doi:10.1186/s40645-023-00534-6.

[9] U. Ranieri, S. D. Cataldo, M. Rescigno, L. Monacelli, R. Gaal, M. Santoro, L. Andriambariarijaona, P. Parisiades, C. D. Michele, L. E. Bove, Observation of the most h₂-dense filled ice under high pressure, Proceedings of the National Academy of Sciences 120 (52) (2023) e2312665120. arXiv:https://www.pnas.org/doi/pdf/10.1073/pnas.2312665120, doi:10.1073/pnas.2312665120.
URL https://www.pnas.org/doi/abs/10.1073/pnas.2312665120

[10] M. J. Russell, L. M. Barge, R. Bhartia, D. Bocanegra, P. J. Bracher, E. Branscomb, R. Kidd, S. McGlynn, D. H. Meier, W. Nitschke, et al., The drive to life on wet and icy worlds, Astrobiology 14 (4) (2014) 308–343.

[11] R. Pierrehumbert, E. Gaidos, Hydrogen greenhouse planets beyond the habitable zone, The Astrophysical Journal Letters 734 (1) (2011) L13.

[12] R. T. Pierrehumbert, The runaway greenhouse on sub-neptune waterworlds, The Astrophysical Journal 944 (1) (2023) 20.

[13] M. Holmberg, N. Madhusudhan, Possible hycean conditions in the sub-neptune toi-270 d, Astronomy & Astrophysics 683 (2024) L2.

[14] N. F. Wogan, N. E. Batalha, K. J. Zahnle, J. Krissansen-Totton, S.-M. Tsai, R. Hu, Jwst observations of k2-18b can be explained by a gas-rich mini-neptune with no habitable surface, The Astrophysical Journal Letters 963 (1) (2024) L7.

[15] Y. A. Dyadin, E. G. Larionov, A. Y. Manakov, F. V. Zhurko, E. Y. Aladko, T. V. Mikina, V. Y. Komarov, Clathrate hydrates of hydrogen and neon, Mendeleev communications 9 (5) (1999) 209–210.

[16] W. L. Mao, H. kwang Mao, A. F. Goncharov, V. V. Struzhkin, Q. Guo, J. Hu, J. Shu, R. J. Hemley, M. Somayazulu, Y. Zhao, Hydrogen clusters in clathrate hydrate, Science 297 (5590) (2002) 2247–2249. arXiv:https://www.science.org/doi/pdf/10.1126/science.1075394, doi:10.1126/science.1075394.
URL https://www.science.org/doi/abs/10.1126/science.1075394

[17] V. Efimchenko, M. Kuzovnikov, V. Fedotov, M. Sakharov, S. Simonov, M. Tkacz, New phase in the water–hydrogen system, Journal of Alloys and Compounds 509 (2011) S860–S863, proceedings of the 12th International Symposium on Metal-Hydrogen Systems, Fundamentals and Applications (MH2010). doi:https://doi.org/10.1016/j.jallcom.2010.12.200.
URL https://www.sciencedirect.com/science/article/pii/S0925838811000107

[18] T. A. Strobel, M. Somayazulu, S. V. Sinogeikin, P. Dera, R. J. Hemley, Hydrogen-stuffed, quartz-like water ice, Journal of the American Chemical Society 138 (42) (2016) 13786–13789, pMID: 27540626. arXiv:https://doi.org/10.1021/jacs.6b06986, doi:10.1021/jacs.6b06986.
URL https://doi.org/10.1021/jacs.6b06986

[19] L. del Rosso, F. Grazzi, M. Celli, D. Colognesi, V. Garcia-Sakai, L. Ulivi, Refined structure of metastable ice xvii from neutron diffraction measurements, The Journal of Physical Chemistry C 120 (47) (2016) 26955–26959.

[20] M. Kuzovnikov, M. Tkacz, T–p–x phase diagram of the water–hydrogen system at pressures up to 10 kbar, The Journal of Physical Chemistry C 123 (6) (2019) 3696–3702.

[21] W. L. Vos, L. W. Finger, R. J. Hemley, H. kwang Mao, Pressure dependence of hydrogen bonding in a novel h2o:h2 clathrate, Chemical Physics Letters 257 (5) (1996) 524–530. doi:https://doi.org/10.1016/0009-2614(96)00583-0.
URL https://www.sciencedirect.com/science/article/pii/0009261496005830

[22] R. L. McFarlan, The Structure of Ice II, The Journal of Chemical Physics 4 (1) (1936) 60–64. arXiv:https://pubs.aip.org/aip/jcp/article-pdf/4/1/60/18788959/60_1_online.pdf, doi:10.1063/1.1749748.
URL https://doi.org/10.1063/1.1749748

[23] Y. Wang, K. Glazyrin, V. Roizen, A. R. Oganov, I. Chernyshov, X. Zhang, E. Greenberg, V. B. Prakapenka, X. Yang, S.-q. Jiang, A. F. Goncharov, Novel hydrogen clathrate hydrate, Phys. Rev. Lett. 125 (2020) 255702. doi:10.1103/PhysRevLett.125.255702.
URL https://link.aps.org/doi/10.1103/PhysRevLett.125.255702

[24] S.-i. Machida, H. Hirai, T. Kawamura, Y. Yamamoto, T. Yagi, Structural changes of filled ice Ic structure for hydrogen hydrate under high pressure, The Journal

of Chemical Physics 129 (22) (2008) 224505. arXiv:https://pubs.aip.org/aip/jcp/article-pdf/doi/10.1063/1.3013440/15421221/224505_1_online.pdf, doi:10.1063/1.3013440.
URL https://doi.org/10.1063/1.3013440

[25] J. Zhang, J.-L. Kuo, T. Iitaka, First principles molecular dynamics study of filled ice hydrogen hydrate, The Journal of Chemical Physics 137 (8) (2012) 084505. arXiv:https://pubs.aip.org/aip/jcp/article-pdf/doi/10.1063/1.4746776/13989271/084505_1_online.pdf, doi:10.1063/1.4746776.
URL https://doi.org/10.1063/1.4746776

[26] H. Hirai, S. Kagawa, T. Tanaka, T. Matsuoka, T. Yagi, Y. Ohishi, S. Nakano, Y. Yamamoto, T. Irifune, Structural changes of filled ice Ic hydrogen hydrate under low temperatures and high pressures from 5 to 50 GPa, The Journal of Chemical Physics 137 (7) (2012) 074505. arXiv:https://pubs.aip.org/aip/jcp/article-pdf/doi/10.1063/1.4746017/15452739/074505_1_online.pdf, doi:10.1063/1.4746017.
URL https://doi.org/10.1063/1.4746017

[27] J. Lei, J. Lim, M. Kim, C.-S. Yoo, Crystal structure of symmetric ice x in h2o–h2 and h2o–he under pressure, The Journal of Physical Chemistry Letters 12 (19) (2021) 4707–4712, pMID: 33979522. arXiv:https://doi.org/10.1021/acs.jpclett.1c00606, doi:10.1021/acs.jpclett.1c00606.
URL https://doi.org/10.1021/acs.jpclett.1c00606

[28] G.-R. Qian, A. O. Lyakhov, Q. Zhu, A. R. Oganov, X. Dong, Novel hydrogen hydrate structures under pressure, Scientific Reports 4 (1) (2014) 5606. doi:10.1038/srep05606.
URL https://doi.org/10.1038/srep05606

[29] B. L. M. d. S. Klotz, Th. Strassle, T. Hansen, High pressure neutron diffraction to beyond 20 gpa and below 1.8 k using paris-edinburgh load frames, High Pressure Research 36 (1) (2016) 73–78. arXiv:https://doi.org/10.1080/08957959.2015.1136624, doi:10.1080/08957959.2015.1136624.
URL https://doi.org/10.1080/08957959.2015.1136624

[30] T. C. Hansen, P. F. Henry, H. E. Fischer, J. Torregrossa, P. Convert, The d20 instrument at the ill: a versatile high-intensity two-axis neutron diffractometer, Measurement Science and Technology 19 (3) (2008) 034001. doi:10.1088/0957-0233/19/3/034001.
URL https://dx.doi.org/10.1088/0957-0233/19/3/034001

[31] W. L. Vos, L. W. Finger, R. J. Hemley, H.-k. Mao, Novel h_2-h_2o clathrates at high pressures, Phys. Rev. Lett. 71 (1993) 3150–3153. doi:10.1103/PhysRevLett.71.3150.
URL https://link.aps.org/doi/10.1103/PhysRevLett.71.3150

[32] T. A. Strobel, M. Somayazulu, R. J. Hemley, Phase behavior of h2 + h2o at high pressures and low temperatures, The Journal of Physical Chemistry C 115 (11) (2011) 4898–4903. arXiv:https://doi.org/10.1021/jp1122536, doi:10.1021/jp1122536.
URL https://doi.org/10.1021/jp1122536

[33] C. G. Salzmann, P. G. Radaelli, E. Mayer, J. L. Finney, Ice xv: A new thermodynamically stable phase of ice, Phys. Rev. Lett. 103 (2009) 105701. doi:10.1103/PhysRevLett.103.105701.
URL https://link.aps.org/doi/10.1103/PhysRevLett.103.105701

[34] U. Ranieri, M. M. Koza, W. F. Kuhs, R. Gaal, S. Klotz, A. Falenty, D. Wallacher, J. Ollivier, P. Gillet, L. E. Bove, Quantum dynamics of h2 and d2 confined in hydrate structures as a function of pressure and temperature, The Journal of Physical Chemistry C 123 (3) (2019) 1888–1903. arXiv:https://doi.org/10.1021/acs.jpcc.8b11606, doi:10.1021/acs.jpcc.8b11606.
URL https://doi.org/10.1021/acs.jpcc.8b11606

[35] C. Prescher, V. B. Prakapenka, Dioptas: a program for reduction of two-dimensional x-ray diffraction data and data exploration, High Pressure Research 35 (3) (2015) 223–230. arXiv:https://doi.org/10.1080/08957959.2015.1059835, doi:10.1080/08957959.2015.1059835.
URL https://doi.org/10.1080/08957959.2015.1059835

[36] J. Rodríguez-Carvajal, Recent advances in magnetic structure determination by neutron powder diffraction, Phys. B Condens. Matter 192 (1) (1993) 55–69. doi:https://doi.org/10.1016/0921-4526(93)90108-I.
URL https://www.sciencedirect.com/science/article/pii/092145269390108I

[37] Y. Fei, A. Ricolleau, M. Frank, K. Mibe, G. Shen, V. Prakapenka, Toward an internally consistent pressure scale, Proceedings of the National Academy of Sciences 104 (22) (2007) 9182–9186. arXiv:https://www.pnas.org/doi/pdf/10.1073/pnas.0609013104, doi:10.1073/pnas.0609013104.
URL https://www.pnas.org/doi/abs/10.1073/pnas.0609013104

[38] H. Hirai, S. Ohno, T. Kawamura, Y. Yamamoto, T. Yagi, Changes in vibration modes of hydrogen and water molecules and in lattice parameters with pressure for filled-ice hydrogen hydrates, The Journal of Physical Chemistry C 111 (1) (2007) 312–315. arXiv:https://doi.org/10.1021/jp064281u, doi:10.1021/jp064281u.
URL https://doi.org/10.1021/jp064281u

[39] P. H. B. Brant Carvalho, A. Mace, I. M. Nangoi, A. A. Leitão, C. A. Tulk, J. J. Molaison, O. Andersson, A. P. Lyubartsev, U. Häussermann, Exploring high-pressure transformations in low-z (h2, ne) hydrates at low temperatures, Crystals 12 (1) (2022). doi:10.3390/cryst12010009.
URL https://www.mdpi.com/2073-4352/12/1/9

[40] A. D. Fortes, I. G. Wood, M. Alfredsson, L. Vočadlo, K. S. Knight, The incompressibility and thermal expansivity of D_2O ice II determined by powder neutron diffraction, Journal of Applied Crystallography 38 (4) (2005) 612–618. doi:10.1107/S0021889805014226.
URL https://doi.org/10.1107/S0021889805014226

[41] F. Datchi, P. Loubeyre, R. LeToullec, Extended and accurate determination of the melting curves of argon, helium, ice (h_2O), and hydrogen (h_2), Phys. Rev. B 61 (2000) 6535–6546. doi:10.1103/PhysRevB.61.6535.
URL https://link.aps.org/doi/10.1103/PhysRevB.61.6535

[42] A. Bondi, van der waals volumes and radii, the Journal of Physical Chemistry 66 (1964) 441.
URL https://pubs.acs.org/doi/pdf/10.1021/j100785a001

[43] S. M. Asuka Harada, Yudha Arman, Molecular dynamics study on fast diffusion of hydrogen molecules in filled ice

ii, Journal of Molecular Liquids 292 (2019) 111316. doi:https://doi.org/10.1016/j.molliq.2019.111316.
URL https://www.sciencedirect.com/science/article/pii/S0167732219323566

[44] S. Klotz, K. Komatsu, H. Kagi, K. Kunc, A. Sano-Furukawa, S. Machida, T. Hattori, Bulk moduli and equations of state of ice vii and ice viii, Phys. Rev. B 95 (2017) 174111. doi:10.1103/PhysRevB.95.174111.
URL https://link.aps.org/doi/10.1103/PhysRevB.95.174111

[45] M. Ahart, M. Somayazulu, S. A. Gramsch, R. Boehler, H.-k. Mao, R. J. Hemley, Brillouin scattering of H2O ice to megabar pressures, The Journal of Chemical Physics 134 (12) (2011) 124517. arXiv:https://pubs.aip.org/aip/jcp/article-pdf/doi/10.1063/1.3557795/15436628/124517_1_online.pdf, doi:10.1063/1.3557795.
URL https://doi.org/10.1063/1.3557795

[46] A. S. J. Méndez, F. Trybel, R. J. Husband, G. Steinle-Neumann, H.-P. Liermann, H. Marquardt, Bulk modulus of h_2O across the ice vii–ice x transition measured by time-resolved x-ray diffraction in dynamic diamond anvil cell experiments, Phys. Rev. B 103 (2021) 064104. doi:10.1103/PhysRevB.103.064104.
URL https://link.aps.org/doi/10.1103/PhysRevB.103.064104

[47] J. S. Zhang, M. Hao, Z. Ren, B. Chen, The extreme acoustic anisotropy and fast sound velocities of cubic high-pressure ice polymorphs at Mbar pressure, Applied Physics Letters 114 (19) (2019) 191903. arXiv:https://pubs.aip.org/aip/apl/article-pdf/doi/10.1063/1.5096989/13623934/191903_1_online.pdf, doi:10.1063/1.5096989.
URL https://doi.org/10.1063/1.5096989

[48] R. Jeanloz, Finite-strain equation of state for high-pressure phases, Geophysical Research Letters 8 (12) (1981) 1219–1222. arXiv:https://agupubs.onlinelibrary.wiley.com/doi/pdf/10.1029/GL008i012p01219, doi:https://doi.org/10.1029/GL008i012p01219.
URL https://agupubs.onlinelibrary.wiley.com/doi/abs/10.1029/GL008i012p01219

[49] R. E. Gagnon, H. Kiefte, M. J. Clouter, E. Whalley, Pressure dependence of the elastic constants of ice Ih to 2.8 kbar by Brillouin spectroscopy, The Journal of Chemical Physics 89 (8) (1988) 4522–4528. arXiv:https://pubs.aip.org/aip/jcp/article-pdf/89/8/4522/18972510/4522_1_online.pdf, doi:10.1063/1.454792.
URL https://doi.org/10.1063/1.454792

[50] G. Tobie, D. Gautier, F. Hersant, Titan's bulk composition constrained by cassini-huygens: implication for internal outgassing, The Astrophysical Journal 752 (2) (2012) 125.

[51] R. L. Kirk, D. J. Stevenson, Thermal evolution of a differentiated ganymede and implications for surface features, Icarus 69 (1) (1987) 91–134.

[52] K. Nagel, D. Breuer, T. Spohn, A model for the interior structure, evolution, and differentiation of callisto, Icarus 169 (2) (2004) 402–412.

[53] G. Tobie, J. I. Lunine, C. Sotin, Episodic outgassing as the origin of atmospheric methane on titan, Nature 440 (7080) (2006) 61–64.

[54] A. Zandanel, R. Hellmann, L. Truche, V. Roddatis, M. Mermoux, G. Choblet, G. Tobie, Geologically rapid aqueous mineral alteration at subfreezing temperatures in icy worlds, Nature Astronomy 6 (5) (2022) 554–559.